Pressure-induced phase transitions in Na 2 B 12 H 12 , structural investigation on a candidate for solid-state electrolyte

Romain Moury, Zbigniew Łodziana, Arndt Remhof, Léo Duchêne, Elsa Roedern, Angelina Gigante, Hans Hagemann

Pressure-induced phase transitions in $Na_2B_{12}H_{12}$, structural investigation on a candidate for solid-state electrolyte

Authors

Romain Moury[ab]*, Zbigniew Łodziana[c], Arndt Remhof[d], Léo Duchêne[da], Elsa Roedern[d], Angelina Gigante[a] and Hans Hagemann[a]

[a]Physical Chemistry, University of Geneva, 30 Quai E. Asermet, Geneva, 1211, Switzerland

[b]b Institut des Molécules et Matériaux du Mans, University of le Mans, Avenue Olivier Messiaen, Le Mans, 72085, France

[c]Institute of Nuclear Physics, Polish Academy of Sciences, ul. Radzikowskiego 152, Kraków, 31342, Poland

[d]EMPA, Swiss Federal Laboratories for Materials Science and Technology, Überlandstrasse 129, Dübendorf, 8600, Switzerland

Correspondence email: romain.moury@univ-lemans.fr

Abstract *Closo*-borates such as $Na_2B_{12}H_{12}$ are an emerging class of ionic conductors that show promising chemical, electro-chemical, and mechanical properties as electrolytes in all-solid-state batteries. Motivated by theoretical predictions, we performed high pressure in situ powder X-ray diffraction on $Na_2B_{12}H_{12}$ and discovered two high pressure phases. The first phase transition occurs at 0.5 GPa and it is persistent at ambient pressure, whereas the second transition takes place between 5.7 and 8.1 GPa and it is fully reversible. We unveil the mechanisms of the transitions by means of group theoretical analysis. The primary order parameters are identified and the stability at ambient pressure of the first polymorph is explained by density functional theory calculations. Finally, we report parameters relevant to engineer and build an all-solid-state battery namely, the bulk modulus and the coefficient of the thermal expansion. The relatively low value of the bulk modulus for the first polymorph (14 GPa) indicates a soft material which allows accommodation of the volume change of the cathode during cycling.

1. Introduction

All-solid-state batteries have a promising future for the next generation of batteries as their performance of solid electrolytes may exceed the thermal and electrochemical stability of liquid electrolytes. They also exhibit transference numbers (ratio of electrical current derived by the cation) close to unity which enable higher power and energy density than batteries based on liquid electrolytes. Furthermore, solid state batteries promise higher operational safety as they overcome the use of a flammable liquid electrolyte and leakages are prevented (Choi & Aurbach, 2016). However solid-state electrolytes usually have low ionic conductivity and reduced contact area with the electrodes hindering their development in real life applications (Choi & Aurbach, 2016). There is a promising, yet under investigated, new class of solid-state electrolytes, namely the *closo*-borates and

related compounds, that combine high conductivity with electrochemical and thermal stability. Up to now, the conduction mechanism in these materials is not known in detail. For the sodium and lithium salts these materials display a common feature: they undergo to a structural phase transition, driven by the temperature, to a dense (often close packed) structure that is highly conductive (Udovic, Matsuo, Unemoto, *et al.*, 2014, Tang *et al.*, 2015, Udovic, Matsuo, Tang, *et al.*, 2014, Tang, Matsuo, Wu, Stavila, Zhou, *et al.*, 2016). For instance, sodium dodecahydro-*closo*-dodecaborate ($Na_2B_{12}H_{12}$) adopts a body centered cubic (bcc) packing at 529K allowing a super ionic conductivity of 0.1 S/cm (Udovic, Matsuo, Unemoto, *et al.*, 2014). As this temperature is too high for practical applications, different strategies have been proposed in order to decrease this temperature (He *et al.*, 2015, Sadikin *et al.*, 2015, Tang, Yoshida, *et al.*, 2016, Duchene, Kuhnel, Rentsch, *et al.*, 2017). One of them, anion mixing, led to the discovery of a solid-electrolyte based on a solid-solution of deca- and dodecaborate ($Na_4[(B_{12}H_{12})(B_{10}H_{10})]$). This material has a high ionic conductivity of 0.9 mS/cm at room temperature, exceeding the ones of its precursors by orders of magnitude (Udovic, Matsuo, Unemoto, *et al.*, 2014, Duchene, Kuhnel, Rentsch, *et al.*, 2017). Combined with an impregnation technique to enhance the contact between electrolyte and cathode material, a stable all-solid-state 3V battery with excellent capacity and cyclability has been demonstrated (Duchene, Kuhnel, Stilp, *et al.*, 2017). Furthermore, recently Moury et al have shown that $Na_2B_{12}H_{12}$ can be prepared in a 3 steps synthesis starting from the cheapest borohydride: $NaBH_4$ decreasing the price of production and making this materials available for further studies (Moury *et al.*, 2017).

At ambient pressure and room temperature, $Na_2B_{12}H_{12}$ crystallizes in a monoclinic $P2_1/c$ space group, replacing the $[B_{12}H_{12}]^{2-}$ anion by the smaller $[B_{10}H_{10}]^{2-}$ anion to get the solid solution $Na_4[(B_{12}H_{12})(B_{10}H_{10})]$, resulting face centred cubic packing (Duchene, Kuhnel, Rentsch, *et al.*, 2017), can be interpreted as adding chemical pressure within the structure of $Na_2B_{12}H_{12}$. Furthermore, Aniya presented a criteria about superconducting materials that should undergo to a structural phase transition at low pressure (Aniya, 1992), and several reports have shown that some superionic conductor do undergo to a structural phase transition at relatively low pressure, this criteria was confirmed in several reports (see (Hull, 2004) and references therein). Motivated by these, we studied the structural evolution of $Na_2B_{12}H_{12}$ upon pressure, in order to verify this behaviour in the class of *closo*-borates.

Interestingly, we observed a rich phase diagram and report two new high-pressure polymorphs for $Na_2B_{12}H_{12}$ with the following transition sequence: $P2_1/c$ (α-polymorph) → *Pbca* (ε-polymorph) → *Pnnm* (ζ-polymorph). The first transition was indeed recorded at relatively low pressures: between 0.3 and 0.5GPa, confirming the criteria proposed by Aniya (Aniya, 1992). The second transition occurs at higher pressure between 5.7 and 8.1 GPa. We discuss and compare the structure in detail. By means of group theoretical analysis we identify the primary order parameters for the transitions. We performed density functional theory (DFT) calculations on $Na_2B_{12}H_{12}$ which revealed that the *Pbca*

symmetry is the most stable compound over a broad range of pressures which is experimentally observed by the irreversibility of the first transition ($P2_1/c$ (α-polymorph) → *Pbca* (ε-polymorph)). Finally, using experimental data combined with DFT calculations we have extracted the bulk and shear modulus and the coefficient of the thermal expansion (CTE) for $Na_2B_{12}H_{12}$, which are important parameters for the design of an all-solid-state battery.

2. Experimental section

2.1. Powder X-Ray diffraction

Sodium dodecahydro-*closo*-dodecaborate ($Na_2B_{12}H_{12}$) powder was purchased from Katchem company. The sample was measured at the Swiss-Norwegian Beam Lines of the European Synchrotron Radiation Facility in Grenoble, France. A 2D image plate detector Pilatus 2M placed at 411 mm from the sample was used with a wavelength of 0.71414 Å. The 2D diffraction patterns were integrated with Bubble software (Dyadkin *et al.*, 2016). The sample detector geometry was calibrated with a LaB_6 NIST standard. The Diamond Anvil Cell (DAC), with flat culet of diameter 600 μm, was loaded in an argon filled glove box (MBraun O_2<0.1 ppm, H_2O<0.1ppm). The sample was loaded together with ruby crystals, for pressure calibration, into a hole of 250 μm drilled in a stainless-steel gasket. No pressure transmitting media was used owing to the low bulk modulus of these families of materials.

For the first transition, indexing of the diffraction pattern was performed using N-TREOR (Altomare *et al.*, 2000) algorithm in EXPO program (Altomare *et al.*, 2013). The space group was verified with Addsym program in Platon package (Spek, 2009). The crystal structure of the ε-phase was solved by direct space method with parallel tempering algorithm implemented in the FOX program (Favre-Nicolin & Cerny, 2002) the refinement was achieved by Rietveld method (Rielveld, 1969) using TOPAS program (Coelho, 2000). The comparison between calculated and experimental diffraction patterns is displayed in Figure S1a. After the refinement, the following agreement factors were obtained, Rwp = 6.6 %, Rp = 9.6 % (background corrected), and GOF = 2.9. The final position for boron and hydrogen were optimized using DFT calculation (see below for details).

For the ζ-$Na_2B_{12}H_{12}$, the structure was found by DFT calculation (see below for details) with a *Pnnm* (No. 58) space group with a = 6.3039(6)Å; b = 8.6652(16)Å and c = 7.0161(19)Å and using the Rietveld method with TOPAS we compared the theoretical pattern with the experimental one in order to validate the structure, during refinement only the sodium positions were refined to get a better agreement. The comparison between calculated and experimental patterns is shown in Figure S1b. The following agreement factors were obtained after refinement Rwp = 6.9%, Rp = 8% (background corrected) and GOF = 2.3.

2.2. Raman

Raman spectra were collected in a diamond anvil cell by a Renishaw 1000 spectrometer with 633 nm excitation laser. The pressure was monitored using an internal ruby standard. The spectra were recorded between 500 cm^{-1} and 2700 cm^{-1}.

2.3. DFT Calculation

DFT calculations were performed in order to resolve the structure of ζ-polymorph; to refine the crystal structure of the high-pressure ε-polymorph, and to determine their thermodynamic properties. The electronic ground state energy was calculated with plane wave formulation of the DFT method implemented in Vienna *ab initio* Simulation Package (VASP) (Kresse & Furthmueller, 1996). The electronic configurations of $1s^1$ for H, $2s^2 2p^1$ for B, and $2p^6 3s^1$ for Na were represented by projected augmented wave potentials (Kresse & Joubert, 1999). The gradient corrected (GGA) exchange-correlation functional and the non-local correction accounting for weak dispersive interactions were applied. Both exchange and correlation electron density was based on revPBE functional (Perdew *et al.*, 1996, Dion *et al.*, 2004).

All considered crystal structures were optimized with respect to the internal atomic positions as well as the unit cell parameters. For the highest pressure phase, an extensive structure search was performed considering the candidate structures with ion packing based on cubic closed pack (ccp), body centered cubic (bcc), hexagonal closed pack (hcp), as well as structures based on Ag_2S (ICSD #262634), Co_2Si (ICSD # 44858); Cu_2O (ICSD #190598). For each candidate structure the initial specific volume per formula unit was 200 $Å^3$. Each structure was optimized (i) with respect to the orientation of anions (ii) cation positions within the unit cell and (iii) with respect to the shape of the unit cell. Each optimized structure was subjected to the simulated annealing (heating to 350K with the rate of 100K/ps, cooling with the rate of 50K/ps); and final re-optimization of the internal degrees of freedom. The symmetry was analyzed for the final structures (Stokes & Hatch, 2005). When new symmetry was found, the structures were re-optimized with the symmetry constraints.

The charge of ions was analyzed with Bader method (Henkelman *et al.*, 2006), the normal modes and the elastic properties were calculated with the finite displacement method (Hector *et al.*, 2007). The bulk modulus is calculated as the average of Voigt and Reuss moduli (Hill, 1952).

3. Results and Discussion

3.1. High pressure crystal structures

The convention describe in Table 1 will be used in the following discussion. The ambient polymorph is denoted α, the three high temperature polymorphs described therein (Verdal *et al.*, 2014) are denoted β, γ, and δ respectively. Temperature phase transition will be discussed in the last section.

Table 1 Summary of the different polymorph known for $Na_2B_{12}H_{12}$ up to know with their temperature and pressure stability range.

Polymorph	α	β	γ	δ	ε	ζ
Space group	*P*2$_1$/*c*	*Pm*-3*n*	*Im*-3*m*	*Fm*-3*m*	*Pbca*	*Pnnm*
a	7.083915	8.05511	8.134716	10.3950	9.71959	6.30201
b	10.747533	8.05511	8.134716	10.3950	10.8522	8.67046
c	9.714884	8.05511	8.134716	10.3950	9.22670	7.01125
β	133.10928	X	X	X	X	X
T range[1]	RT-540K	511-587K	587-700K	587-700K	X	X
P range[2]	0-0.5GPa	X	X	X	0.5-5.7GPa[3]	>8.1GPa

[1] at ambient pressure and [2] at room temperature.

In this work, we report two pressure induced phase transitions at RT for the α-$Na_2B_{12}H_{12}$.The first pressure induced transition occurs between 0.3 and 0.5 GPa. The second transition is observed between 5.4 and 8.1GPa (Figure 1a). The crystal structure of this phase was determined by simulated annealing global energy minimum search to have an orthorhombic *Pnnm* (ζ-phase) symmetry, as shown in Figure S2. As it can be inferred from Figure 1b, the transition ε → ζ is fully reversible and it has a hysteresis. By contrast, the transition α → ε is irreversible or has a large hysteresis as it can be seen in Figure 1b, the ε-phase remains at ambient pressure.

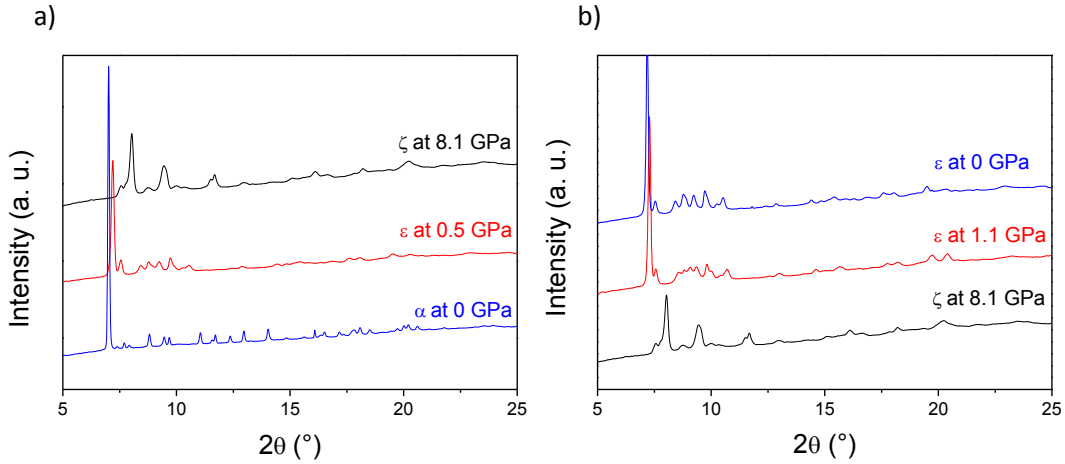

Figure 1 High pressure in situ PXD patterns of $Na_2B_{12}H_{12}$ a) during compression: bleu diffraction pattern *P*2$_1$/*c* (0GPa, α-polymorph), red diffraction pattern *Pbca* (0.5GPa ε-polymorph) and black diffraction pattern *Pnnm* (8.1GPa, ζ-polymorph) and b) during decompression: black diffraction pattern *Pnnm* (8.1GPa ζ-polymorph), red diffraction pattern *Pbca* (1.1GPa, ε-polymorph) and blue diffraction pattern corresponds to the *Pbca* (0GPa, ε-polymorph) at ambient pressure (showing the irreversibility).

The variation of the volume as a function of the pressure is shown in Figure 2. Considering the volume per formula unit, we estimate a volume collapses of 4.8 % during the transition α → ε. For the transition *Pbca* → *Pnnm*, the volume decreases by 2.1%, smaller than the first transition but high enough to classify the transition as first order. The Murnaghan equation of state (Eq.1) was used to fit the volume change of the ε-polymorph (Murnaghan, 1944).

$$V(P) = V_0 \left(1 + B_0{}' \frac{P}{B_0}\right)^{-1/B_0'} \quad (1)$$

Where V_0 is the volume at 0 pressure, B_0 the bulk modulus, and B_0' the first pressure derivative of B_0. The result is represented in Figure 2. We determined that V_0 = 250.7 ± 0.4 Å^3/formula unit, B_0 = 14.0 ± 0.5 GPa and B_0' = 6.1 ± 0.2. The bulk modulus for ε-$Na_2B_{12}H_{12}$ is lower than $NaBH_4$ revealing a higher compressibility (Kumar & Cornelius, 2005). It is worth to note that, as for $NaBH_4$, no pressure transmitting media was used leading to non-hydrostatic conditions which could tend to overestimate the bulk modulus (Duffy *et al.*, 1999). In fact, Inelastic X-ray scattering has demonstrated to give more accurate values for the bulk modulus in the case of light boron hydrogen compounds (Chernyshov *et al.*, 2008).

In view of potential applications, the high compressibility of ε-$Na_2B_{12}H_{12}$ is beneficial to absorb volume changes of electrodes materials during cycles.

The elastic properties were also calculated for each of high pressure phases at the equilibrium volume, similar as for measurements presented above. For ζ-$Na_2B_{12}H_{12}$ calculated B_0=14.0 GPa; B_0=15.4 GPa for ε- $Na_2B_{12}H_{12}$, and for the low temperature phase with $P2_1/c$ symmetry B_0=17.3 GPa. The shear modulus equals G=3.7 GPa, 6.9 GPa and 3.3 GPa for ζ-, ε-, and α-polymorphs respectively. The shear modulus is small for all compounds. Taking into account polycrystalline nature of the powder sample, the agreement with the experimental data for ε- $Na_2B_{12}H_{12}$ is good (14.0 GPa vs. 15.4 GPa) validating the methodology used for DFT calculation. The previous calculations report B_0=10.52 GPa for α-$Na_2B_{12}H_{12}$ (Lu & Ciucci, 2017). This is a lower value than the present calculations, however different methodology was used in this work. Discrepancies of similar order are noticed for the bulk modulus for $NaBH_4$ reported to vary between 16.27 GPa and 19.27 GPa (Lu & Ciucci, 2017).

Elastic properties close to the normal conditions are of practical interest and the extrapolation to V_0 presented above refers to such situation. With increasing pressure, the bulk modulus increases due to the smaller interatomic distances. Thus, the high pressure ζ-polymorph has the lowest B_0 at the calculated equilibrium volume V_0= 259.9 Å^3/formula unit. With increasing volume B_0 increases reaching values above 30 GPa for volumes ~200 A^3/ formula unit that corresponds to the pressures above transition to the *Pnnm* symmetry.

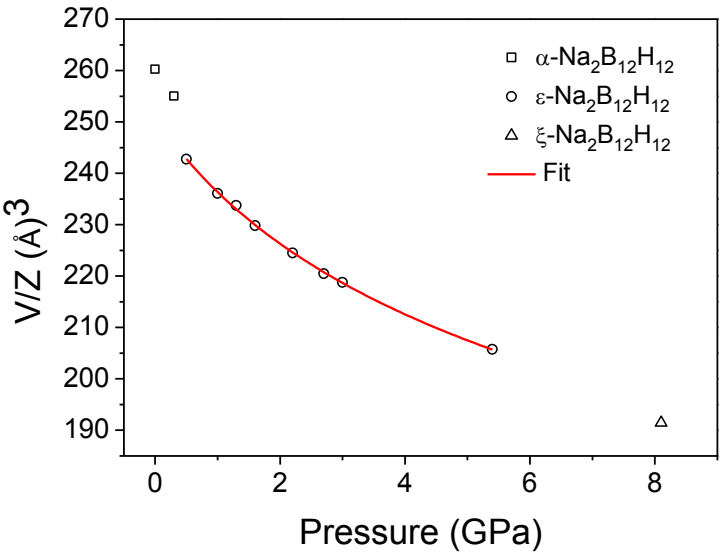

Figure 2 Variation of the volume per formula units as a function of pressure for α-, ε- and ζ-$Na_2B_{12}H_{12}$ and for ε-$Na_2B_{12}H_{12}$ with the fit using Murnaghan equation of state (Eq. 1).

The crystal structure of the ε- and ζ-polymorphs are reported in Figure 3a and 3b respectively. A distorted *fcc*-fashion packing is adopted by the $B_{12}H_{12}^{2-}$ anions in all 3 polymorphs. The transition α → ε is a first order displacive phase transition, with a direct group-subgroup relationship *Pbca* → $P2_1/c$. For the structure comparison, we have transformed the α-phase into a cell with *fcc*-based packing and $P2_1/c$ symmetry using the following transformation matrix: $\mathbf{a}_{fcc,\ mono} = 2\mathbf{a}_{mono} + \mathbf{c}_{mono}$, $\mathbf{b}_{fcc,\ mono} = -\mathbf{b}_{mono}$ and $\mathbf{c}_{fcc,\ mono} = -\mathbf{c}_{mono}$, (Figure S3a). For the second transition, there is no direct group-subgroup relationship between *Pbca* and *Pnnm.* However, for comparison, one can build a distorted *fcc*-based cell using the following transformation matrix: $\mathbf{a}_{fcc,\ mono} = \mathbf{a}_{bcc,\ ortho} + \mathbf{c}_{bcc,\ ortho}$, $\mathbf{b}_{fcc,\ mono} = \mathbf{b}_{bcc,\ ortho}$ and $\mathbf{c}_{fcc,\ mono} = \mathbf{a}_{bcc,\ mono} - \mathbf{c}_{bcc,\ ortho}$ with a splitting of the Wyckoff positions 4g into the two positions 4e give an apparent $P2_1/c$ symmetry within this new cell, which is a subgroup of the *Pbca* (Figure S3b). Hence, the second transition can be described as a 1st order displacive phase transition. It is worth to note that the symmetry for the analogs alkali dodecahydro-*closo*-dodecaborate with cation with higher radii, namely K, Rb and Cs is *Fm*-3 (202) (Tiritiris & Schleid, 2003, Tiritiris *et al.*, 2000) whereas, the symmetry is *Pa*-3 (205) in $Li_2B_{12}H_{12}$ (Her *et al.*, 2008). Interestingly, there is a chain of maximal subgroups from *Fm*-3 to $P2_1/c$ containing all the mentioned symmetries, which is *Fm*-3 → *Pa*-3 → *Pbca* → $P2_1/c$ with a *fcc*-based packing. The *Pbca* symmetry is connected to the higher space groups adopted by the analog alkali dodecahydro-*closo*-dodecaborates at room temperature.

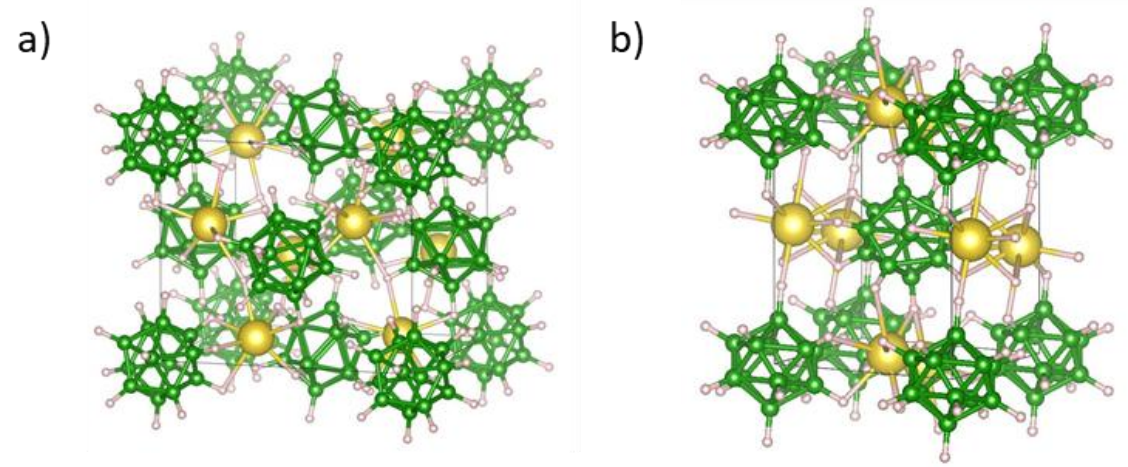

Figure 3 Graphical representation of the crystal structure for a) ε-polymorph (*Pbca*) and b) ζ-polymorph (*Pnnm*): boron (green), hydrogen (white) and sodium (yellow).

In order to describe the mechanisms of the transitions, we performed a group theoretical analysis using AMPLIMODE (Orobengoa *et al.*, 2009, Perez-Mato *et al.*, 2010) in the Bilbao Crystallographic Server (Aroyo *et al.*, 2011, Aroyo, Perez-Mato, *et al.*, 2006, Aroyo, Kirov, *et al.*, 2006). Both transitions combine a diffusionless (martensitic like) transformation and a displacement of sodium. Regarding the diffusionless transformation, in the first transition, the monoclinic lattice is brought into the orthorhombic one, as displayed in Figure 4a, 4b and 4c. The 2nd transition has an orthorhombic lattice transformed into a monoclinic one (Figure 4d, 4e and 4f), combining shrinking and shearing for both transitions. The components of the strain tensor induced by the distortion of the lattice, in α → ε transition, are rather small: e_{11} = -0.0514, e_{22} = 0.0208, e_{33} = -0.0126 and e_{13} = e_{31} = 0.0093. Therefore, we can conclude that the strains do not play an important role. Whereas, the deformation of the orthorhombic lattice has a biaxial behavior in the second transition, and the diagonal components of the strain tensor are: e_{22} = -0.1477 and e_{33} = 0.1342, being an order of magnitude higher than the component e_{11} = -0.0681. Hence, spontaneous strains cannot be neglected in the order parameter for this transition. The second mechanism is the diffusion of Na within the structure. The stability of the distorted structure could be rationalized by identifying the primary distortion modes: unstable modes in the high symmetry structure. The analysis is made for the transitions *Pbca* → $P2_1/c$ (α ← ε → ζ). The group theoretical analysis allowed us to identify two modes, characterized by Γ^{1+} and Γ^{4+} for ε → α (Figure 5a and 5b), and by Γ^{1+} and Γ^{3+} for ε → ζ (Figure 5c and 5d) irreducible representations (irreps) at the Brillouin zone center. The primary modes breaking the symmetry, with $P2_1/c$ as isotropy subgroup, are the Γ^{4+} and Γ^{3+} for the transitions ε → α and ε → ζ respectively. Hence, the primary mode responsible of the stabilization of the distorted structure at ambient pressure is Γ^{4+}. However, the amplitude of this mode is fairly high 2.4 Å, which could explain the non-reversibility of the transition. This result agrees with DFT calculations revealing that *Pbca* symmetry is the most thermodynamically stable compound over a broad range of pressure at 0K (Figure S2). Then, the

*P*2$_1$/*c* symmetry found at RT and ambient pressure could be a metastable phase formed kinetically. It would be interesting to study the influence of the temperature on the ε → α reversibility.

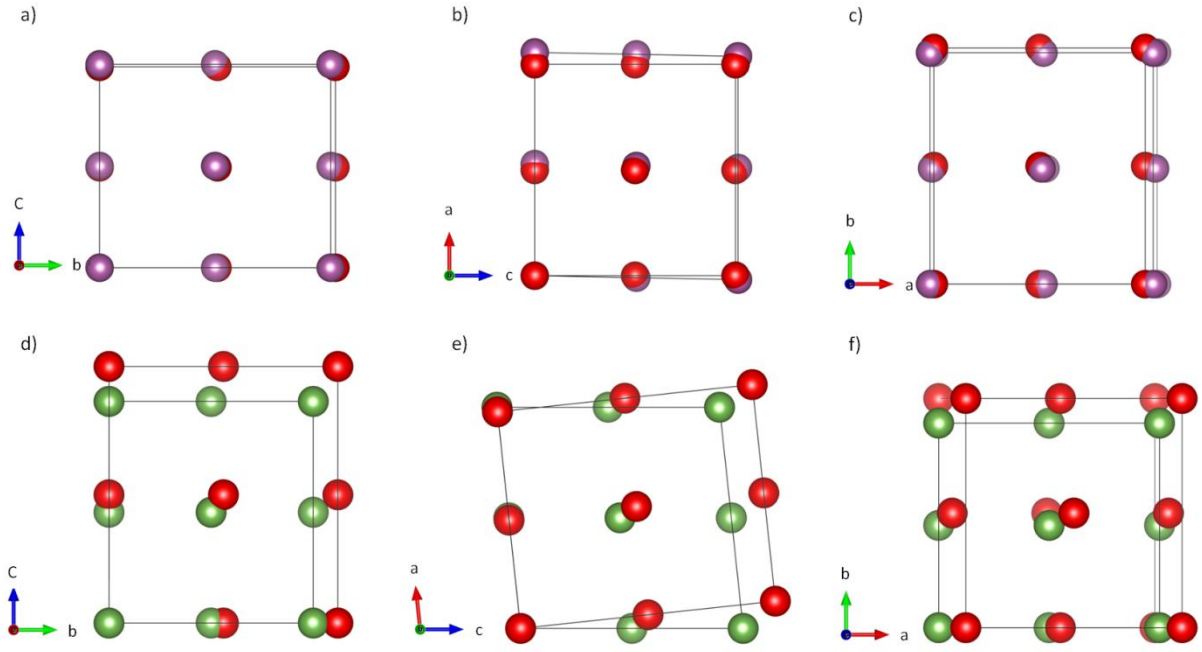

Figure 4 Representation of the transformation of the monoclinic lattice (α-polymorph *PI/c*, purple) into the orthorhombic lattice (ε-polymorph *Pbca*, red) along a) a axis, b) b axis and c) c axis. Representation of the transformation of the orthorhombic lattice (ε-polymorph *Pbca*, red) into the monoclinic lattice (ζ-polymorph *Pnnm*) green) along d) a axis, e) b axis and f) c axis. For the sake of clarity, sodium have been removed and the $B_{12}H_{12}^{2-}$ replaced by spheres.

According to the present DFT calculation, octahedral interstitials are unstable for sodium in α- and ε-$Na_2B_{12}H_{12}$ but they are stable in the ζ-polymorph, the most stable sites being trigonal voids for the former polymorphs. These results are in agreement with the experiments. In fact, sodium are in a trigonal environment slightly out of the plane with improper torsion angles of 11.2° and 12.4° toward the tetrahedral sites in the α-polymorph and of 15.5° and 21.1° toward the octahedral sites in the ε-polymorph. During this transition, sodium are pushed in the direction of the octahedral voids (Figure S4a and S4b), allowing to increase the closest Na-Na distance from 4.46 to 4.57 Å. Regarding the ζ-polymorph, sodium cations get into the octahedral interstitials, their improper torsion angles are in the range of 23-34.3° out of the octahedral facets. Consequently, they tend to form dimers with Na-Na distances of 3.38 and 3.87 Å (Figure S4c). The $B_{12}H_{12}^{2-}$ anions are in distorted octahedron for the 3 polymorphs, the ε-polymorph is the least distorted (Figure S5). The angles between vertices are in the range of: 65.1-114.9° for α-, 86.3-93.7° for ε-, and 50.4-129.6° for ζ- $Na_2B_{12}H_{12}$. The length of the edges is in the range of 4.85-7.03Å, 5.56-6.52Å and 3.30-7.01Å for α-, ε- and ζ-$Na_2B_{12}H_{12}$ respectively. In ε-phase, four of sodium are coordinated to the edges formed by 2 H on $B_{12}H_{12}^{2-}$ and 2 sodium are coordinated through the face formed by 3 H on the $B_{12}H_{12}^{2-}$ unit (Figure S6b). The ζ-

polymorph has four sodium coordinated to the faces and two by the edges (Figure S6c). The α-polymorph has two sodium coordinated through the faces and the other four are in between, tilted from the plan formed by the H-B-B-H edges by about 30° (Figure S6a). The perfect octahedron would be obtained if the 6 sodium are coordinated to the edges of the $B_{12}H_{12}^{2-}$ unit.

Due to some large changes in the local ion environment between high pressure phases, we performed analysis of the bonds through the Bader space partitioning method. All three analyzed phases are strongly ionic with calculated charge on sodium larger than +0.86e. With increasing pressure (decreasing specific volume), the charge on ions reduces for about 2% in the range relevant to our experiments. Interestingly, in ζ- $Na_2B_{12}H_{12}$ due to Na dimer formation the charge on sodium is larger than for other phases at similar volumes. Thus, migration of Na toward the octahedral void and formation of Na-Na dimer allows to preserve ionic character of the compound.

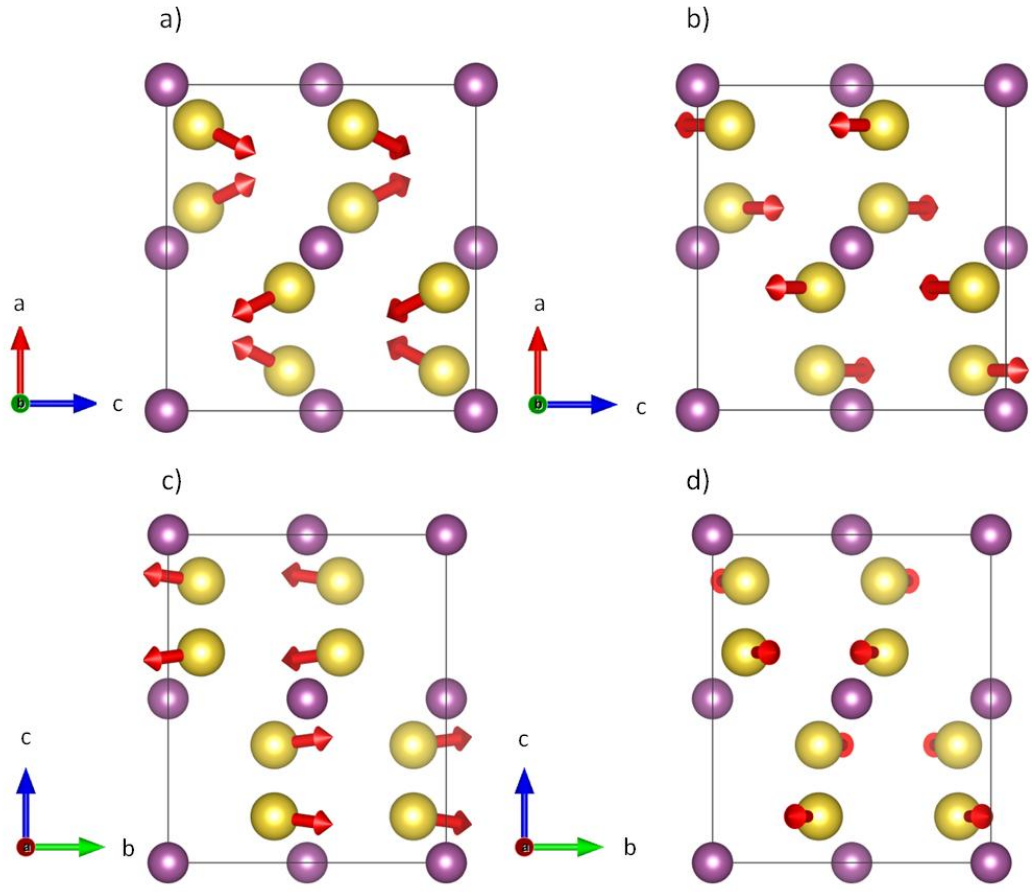

Figure 5 Representation of the symmetry adapted displacive modes describe by the irreps a) Γ^{1+} and b) Γ^{4+} for the transition ε → α and c) Γ^{1+} and d) Γ^{3+} for the transition ε → ζ. The $B_{12}H_{12}^{2-}$ anions are replaced by purple spheres and sodium are in yellow.

It is interesting to specify that a similar phase sequence has been reported previously for ZrO_2 both as a function of temperature and as a function of pressure. These transitions have been discussed in detail using Landau theory and first principle calculations (Fadda *et al.*, 2002, Wang *et al.*, 2015).

4. High pressure vibrational spectra

For isolated $B_{12}H_{12}^{2-}$, six Raman active modes are expected and observed in aqueous solution at 584 (H_g), 743 (A_g), 770(H_g), 949 (H_g), 2475 (H_g) and 2518 (A_g) cm^{-1} (Sethio *et al.*, 2016, Sethio *et al.*, 2017). At room temperature and ambient pressure the site symmetry of the *closo*-borate anion is lowered to C_i, in the monoclinic $Na_2B_{12}H_{12}$ structure. Thus, the fivefold degenerate modes H_g will be split into five components. Experimentally, at ambient pressure, the H_g normal mode around 584 cm^{-1} (Nogi & Tanaka, 2006) is split into two components (579 and 590 cm^{-1}). Two signals are observed at 751 and 768 cm^{-1} (A_g and H_g normal mode respectively), as well as some weaker features. The band expected around 949 cm^{-1} is split into several weak peaks. The B-H stretching mode of the $B_{12}H_{12}^{2-}$ ion shows several components with maxima at 2484, 2503 and 2527 cm^{-1} (corresponding to H_g and A_g stretching modes), see Figure 6.

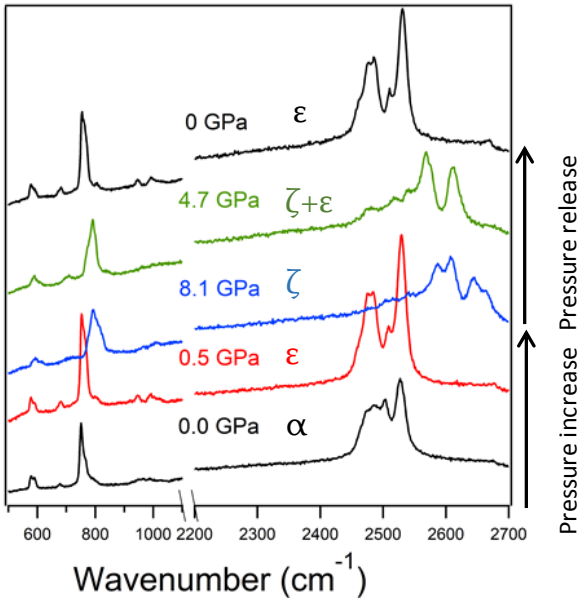

Figure 6 High pressure Raman spectra during compression (black, red and blue lines) and after pressure release (green and black lines).

With increasing pressure, all bands are shifted to higher frequencies owing to B-H bonds contraction. It is worth to emphasise that the magnitude of the pressure shift of the B-H stretching modes (ca. 19 cm^{-1}/GPa) is similar to the one observed in $Cs_2B_{12}H_{12}$ up to 1 GPa (between 16 and 23 cm^{-1}/GPa) (Benham *et al.*, 1987). According to our theoretical calculations, this would correspond to a contraction of the B-H bond of 0.002Å/GPa) (Hagemann *et al.*, 2018). In agreement with X-ray data also the Raman measurements reveal two phase transitions. The first transition appears around 0.5 GPa, while the second one between 5.4 and 8.1 GPa. Figure 6 also shows the effect of pressure release. While the ζ-phase reverts to ε-phase, the α-polymorph is not recovered upon pressure release as shown by the differences in the spectra at 0 GPa before compression and after decompression.

5. High temperature crystal properties

Temperature-induced phase transitions in $Na_2B_{12}H_{12}$ have already been studied (Verdal *et al.*, 2014, Sadikin *et al.*, 2017). Nevertheless, no Coefficient of the Thermal Expansion (CTE) for the low and high temperature (β-polymorph *Pm*-3*n* and γ-polymorph *Im*-3*m*) phases of $Na_2B_{12}H_{12}$ was determined. The CTE is an important parameter to design all-solid-state batteries to minimize detrimental stress at the interface of materials. Hence, we have measured thermal *in-situ* Powder X-ray Diffraction (HT-PXD) to get the CTE. Figure 7 shows the patterns of the HT-PXD experiments. The result is consistent with the report made by Verdal at al. (Verdal *et al.*, 2014) and Sadikin et al. (Sadikin *et al.*, 2017). $Na_2B_{12}H_{12}$ undergoes to two successive order-disorder phase transitions starting at 511 K where the $P2_1/c$ transform into the cubic *Pm*-3*n* phase and both phases coexist until 540 K. The primitive cubic phase is transformed into the more disordered *Im*-3*m* phase at 587 K. Simultaneously, another minor transition into the δ-phase *Fm*-3*m* takes place (see Figure S7 for the attribution of the different phases).

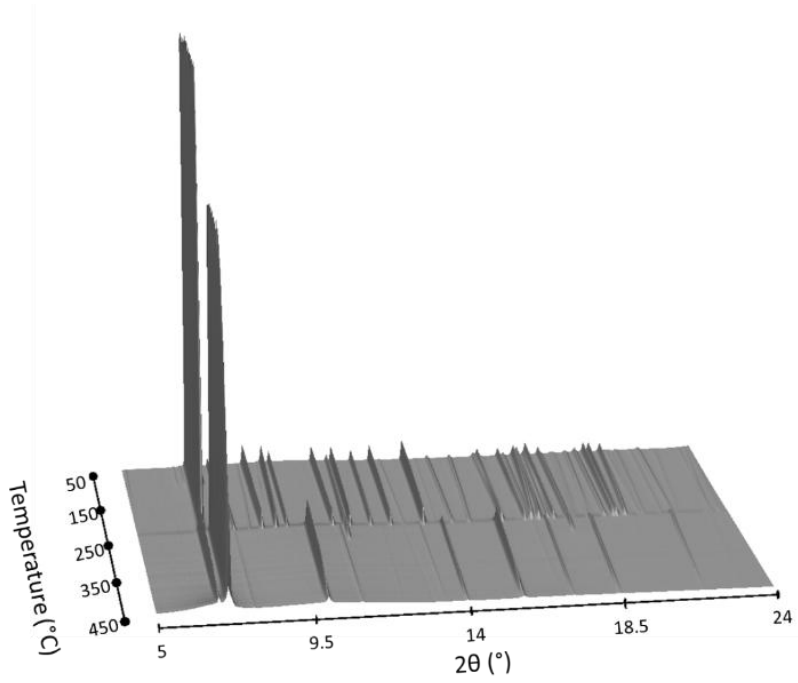

Figure 7 Evolution of $Na_2B_{12}H_{12}$ diffraction patterns with temperature increase.

The expansion of cell parameters as a function of temperature for the RT α-phase may be expressed as a 3rd order polynomial function (Figure S8). The choice of the 3rd order was made by comparing the residual of the fit with different orders until no trend in the residual was observed (Figure S10). Concerning the β- and γ-polymorphs, the volumes V vary linearly with temperature (Figure S9). Table S1 summarized the obtained temperature dependent equations for the three polymorphs. As a result, we could determine the CTE α using Equation 2.

$$\alpha = \frac{1}{V} \times \frac{dV}{dT} \quad (2)$$

Where V is the volume and T the temperature.

Figure 8 shows the evolution of the CTE as a function of temperature of the α-, β- and γ-polymorphs. The average CTE for the α-polymorph is 130.10^{-6} K^{-1} over the range 273-540 K, for β-$Na_2B_{12}H_{12}$ is 230.10^{-6} K^{-1} over the range 540-580 K and is equal to 180.10^{-6} K^{-1} for the γ-phase between 580 and 700K. For the α-phase, the CTE first decreases with temperature until 340 K reaching its minimum value of 111.10^{-6} K^{-1}. Then, the CTE increases smoothly with temperature to come up to 186.10^{-6} K^{-1} at 540°C. Such anomalous evolution of the CTE reveals a lattice anharmonicity at temperatures below the phase transition. At this stage, the α-phase transforms into the β-phase, where the CTE jumps by 22% to 228.10^{-6} K^{-1} and it goes down linearly with temperature to 226.10^{-6} K^{-1} at 580 K, temperature at which the last transition takes place and the CTE drops by 19% to 183.10^{-6} K^{-1} and linearly decreases with temperature to 178.10^{-6} K^{-1}. In Table S2, we summarize the different physical properties of all the polymorphs studied herein.

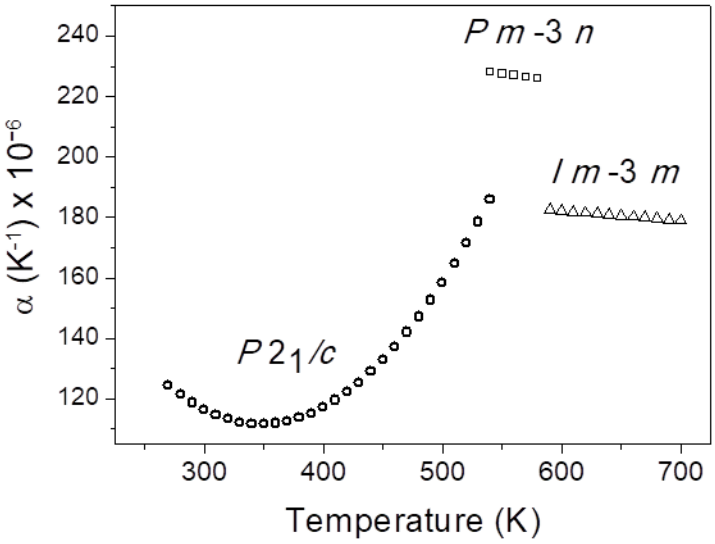

Figure 8 CTE evolution as a function of temperature for the LT- and HT-$Na_2B_{12}H_{12}$.

6. Conclusion

We investigated the high-pressure phase diagram of $Na_2B_{12}H_{12}$, a novel, boron–based sodium superionic conductor. In this study we highlighted that $Na_2B_{12}H_{12}$ has a rich phase diagram and a transition to a relatively low pressure. Indeed, we found two successive phase transitions; first to the ε-$Na_2B_{12}H_{12}$ (*Pbca*) at 0.5 GPa and second to the ζ-$Na_2B_{12}H_{12}$ (*Pnnm*) between 5.7 and 8.1 GPa. The relatively low pressure for the first transition confirms the criterion propose by Aniya (Aniya, 1992) claiming that superionic materials should undergo pressure induced phase transition at low pressure and the reports made on superionic conductor undergoing to phase transition at low pressure (Hull, 2004). Moreover, our *in-situ* XRD data allowed us to determined the bulk modulus, B_0 = 14 GPa, for

the α-polymorph with a striking agreement with the calculated one, B_0 = 15.4 GPa, validating the strategy used for the DFT calculation. The elastic properties of $Na_2B_{12}H_{12}$ reveal a high compressibility for this material which is beneficial to accommodate the volume changes during charge and discharge of the battery.

The mechanism of the transition revealed an interesting formation of a Na-Na dimer by displacement of the sodium from the tetrahedral sites, in the *fcc*-like cell, to the octahedral void in order to preserve the ionic character of the material.

Interestingly, we observed that the ε-polymorph persists at ambient pressure; we explained this phenomenon using group theoretical analysis and DFT calculations. Indeed, we determined the amplitude of the primary order parameter for the transition ε→α being 2.4 Å which is fairly high, furthermore, the stability of the orthorhombic phase was calculated by DFT and revealed that this symmetry is the most stable symmetry over a broad range of pressure.

Finally through the evolution of the cell parameters as a function of the temperature we determined the CTE for this compound which should be of use in the design of an all-solid-state battery.

Acknowledgements We thank V. Dimitriev, I. Dovgaliuk and D. Cheryshov of the SNBL at ESRF for their support with the high pressure experiments. We thank the financial support from the SNSF Sinergia project CRSII2_160749 and the SNSF project 200021_169033/1. Z. Ł. acknowledge NCN project 2015/17/B/ST3/02478 and by CPU allocation at PL-Grid.

References

Altomare, A., Cuocci, C., Giacovazzo, C., Moliterni, A., Rizzi, R., Corriero, N. & Falcicchio, A. (2013). *J. Appl.Cryst.* **46**, 1231-1235.

Altomare, A., Giacovazzo, C., Guagliardi, A., Moliterni, A. G. G., Rizzi, R. & Werner, P.-E. (2000). *J. Appl.Cryst.* **33**, 1180-1186.

Aniya, M. (1992). *Solid State Ionics* **50**, 125-129.

Aroyo, M. I., Kirov, A., Capillas, C., Perez-Mato, J. M. & Wondratschek, H. (2006). *Acta Crystallogr., Sect. A: Found. Crystallogr.* **A62**, 115-128.

Aroyo, M. I., Perez-Mato, J. M., Capillas, C., Kroumova, E., Ivantchev, S., Madariaga, G., Kirov, A. & Wondratschek, H. (2006). *Z. Kristallogr.* **221**, 15-27.

Aroyo, M. I., Perez-Mato, J. M., Orobengoa, D., Tasci, E., de la Flor, G. & Kirov, A. (2011). *Bulg. Chem. Commun.* **43**, 183-197.

Benham, V., Lord, G., Butler, I. S. & Gilson, D. F. R. (1987). *Appl. Spectrosc.* **41**, 915-917.

Chernyshov, D., Bosak, A., Dmitriev, V., Filinchuk, Y. & Hagemann, H. (2008). *Phys. Rev. B: Condens. Matter* **78**, 172104/1-172104/4.

Choi, J. W. & Aurbach, D. (2016). *Nat. Rev. Mater.* **1**, 16013.

Coelho, A. A. (2000). *J. Appl. Crystallogr.* **33**, 899-908.

Dion, M., Rydberg, H., Schroeder, E., Langreth, D. C. & Lundqvist, B. I. (2004). *Phys. Rev. Lett.* **92**, 246401/1-246401/4.

Duchene, L., Kuhnel, R. S., Rentsch, D., Remhof, A., Battaglia, C. & Hagemann, H. (2017). *Chem. Commun.* **53**, 4195-4198.

Duchene, L., Kuhnel, R. S., Stilp, E., Cuervo Reyes, E., Remhof, A., Hagemann, H. & Battaglia, C. (2017). *Energy Environ. Sci.* **10**, 2609-2615.

Duffy, T. S., Shen, G., Heinz, D. L., Shu, J., Ma, Y., Mao, H.-K., Hemley, R. J. & Singh, A. K. (1999). *Phys. Rev. B: Condens. Matter Mater. Phys.* **60**, 15063-15073.

Dyadkin, V., Pattison, P., Dmitriev, V. & Chernyshov, D. (2016). *J. Synchrotron Radiat.* **23**, 825-829.

Fadda, G., Truskinovsky, L. & Zanzotto, G. (2002). *Phys. Rev. B: Condens. Matter* **66**, 174107/1-174107/10.

Favre-Nicolin, V. & Cerny, R. (2002). *J. Appl. Cryst.* **35**, 734-743.

Hagemann, H., Sharma, M., Sethio, D. & Lawson Daku, L. M. (2018). *Helv. Chim. Acta* **101**, e1700239/1- e1700239/5.

He, L., Li, H.-W., Nakajima, H., Tumanov, N., Filinchuk, Y., Hwang, S.-J., Sharma, M., Hagemann, H. & Akiba, E. (2015). *Chem.Mater* **27**, 5483-5486.

Hector, L. G., Herbst, J. F., Wolf, W., Saxe, P. & Kresse, G. (2007). *Phys. Rev. B: Condens. Matter* **76**, 014121.

Henkelman, G., Arnaldsson, A. & Jónsson, H. (2006). *Comput. Mater. Sci.* **36**, 354-360.

Her, J.-H., Yousufuddin, M., Zhou, W., Jalisatgi, S. S., Kulleck, J. G., Zan, J. A., Hwang, S.-J., Bowman, R. C. & Udovic, T. J. (2008). *Inorg. Chem.* **47**, 9757-9759.

Hill, R. (1952). *Proc. Phys. Soc.* **65A**, 349-354.

Hull, S. (2004). *Rep. Prog. Phys.* **67**, 1233-1314.

Kresse, G. & Furthmueller, J. (1996). *Phys. Rev. B: Condens. Matter* **54**, 11169-11186.

Kresse, G. & Joubert, D. (1999). *Phys. Rev. B: Condens. Matter* **59**, 1758-1775.

Kumar, R. S. & Cornelius, A. L. (2005). *Appl. Phys. Lett.* **87**, 261916/1-261916/3.

Lu, Z. & Ciucci, F. (2017). *Chem. Mater.* **29**, 9308-9319.

Moury, R., Gigante, A. & Hagemann, H. (2017). *Int. J. Hydrogen Energy* **42**, 22417-22421.

Murnaghan, F. D. (1944). *Proc. Natl. Acad. Sci.***30**, 244-247.

Nogi, N. & Tanaka, S. (2006). *J. Solid State Chem.* **179**, 2927-2933.

Orobengoa, D., Capillas, C., Aroyo, M. I. & Perez-Mato, J. M. (2009). *J. Appl. Cryst.* **42**, 820-833.

Perdew, J. P., Burke, K. & Ernzerhof, M. (1996). *Phys. Rev. Lett.* **77**, 3865-3868.

Perez-Mato, J. M., Orobengoa, D. & Aroyo, M. I. (2010). *Acta Crystallogr., Sect. A: Found. Crystallogr.* **66**, 558-590.

Rietveld, H. (1969) *J. Appl. Cryst.* **2**, 65-71.

Sadikin, Y., Brighi, M., Schouwink, P. & Cerny, R. (2015). *Adv. Energy Mater.* **5**, 1501016/1-1501016/6.

Sadikin, Y., Schouwink, P., Brighi, M., Lodziana, Z. & Cerny, R. (2017). *Inorg. Chem.* **56**, 5006-5016.

Sethio, D., Lawson Daku, L. M. & Hagemann, H. (2016). *Int. J. Hydrogen Energy* **41**, 6814-6824.

Sethio, D., Lawson Daku, L. M. & Hagemann, H. (2017). *Int. J. Hydrogen Energy* **42**, 22496-22501.

Spek, A. (2009). *Acta Crystallogr., Sect. D* **65**, 148-155.

Stokes, H. T. & Hatch, D. M. (2005). *J. Appl. Crystallogr.* **38**, 237-238.

Tang, W. S., Matsuo, M., Wu, H., Stavila, V., Unemoto, A., Orimo, S.-i. & Udovic, T. J. (2016). *Energy Storage Mater.***4**, 79-83.

Tang, W. S., Matsuo, M., Wu, H., Stavila, V., Zhou, W., Talin, A. A., Soloninin, A. V., Skoryunov, R. V., Babanova, O. A., Skripov, A. V., Unemoto, A., Orimo, S.-i. & Udovic, T. J. (2016). *Adv. Energy Mater.* **6**, 1502237/1- 1502237/6.

Tang, W. S., Unemoto, A., Zhou, W., Stavila, V., Matsuo, M., Wu, H., Orimo, S.-i. & Udovic, T. J. (2015). *Energy Environ. Sci.* **8**, 3637-3645.

Tang, W. S., Yoshida, K., Soloninin, A. V., Skoryunov, R. V., Babanova, O. A., Skripov, A. V., Dimitrievska, M., Stavila, V., Orimo, S.-i. & Udovic, T. J. (2016). *ACS Energy Lett.* **1**, 659-664.

Tiritiris, I. & Schleid, T. (2003). *Z. Anorg. Allg. Chem.* **629**, 1390-1402.

Tiritiris, I., Schleid, T., Muller, K. & Preetz, W. (2000). *Z. Anorg. Allg. Chem.* **626**, 323-325.

Udovic, T. J., Matsuo, M., Tang, W. S., Wu, H., Stavila, V., Soloninin, A. V., Skoryunov, R. V., Babanova, O. A., Skripov, A. V., Rush, J. J., Unemoto, A., Takamura, H. & Orimo, S.-i. (2014). *Adv. Mater.* **26**, 7622-7626.

Udovic, T. J., Matsuo, M., Unemoto, A., Verdal, N., Stavila, V., Skripov, A. V., Rush, J. J., Takamura, H. & Orimo, S.-i. (2014). *Chem. Commun.* **50**, 3750-3752.

Verdal, N., Her, J.-H., Stavila, V., Soloninin, A. V., Babanova, O. A., Skripov, A. V., Udovic, T. J. & Rush, J. J. (2014). *J. Solid State Chem.* **212**, 81-91.

Wang, W., Liang, Z., Han, X., Chen, J., Xue, C. & Zhao, H. (2015). *J. Alloys Compd.* **622**, 504-512.

Supporting Information

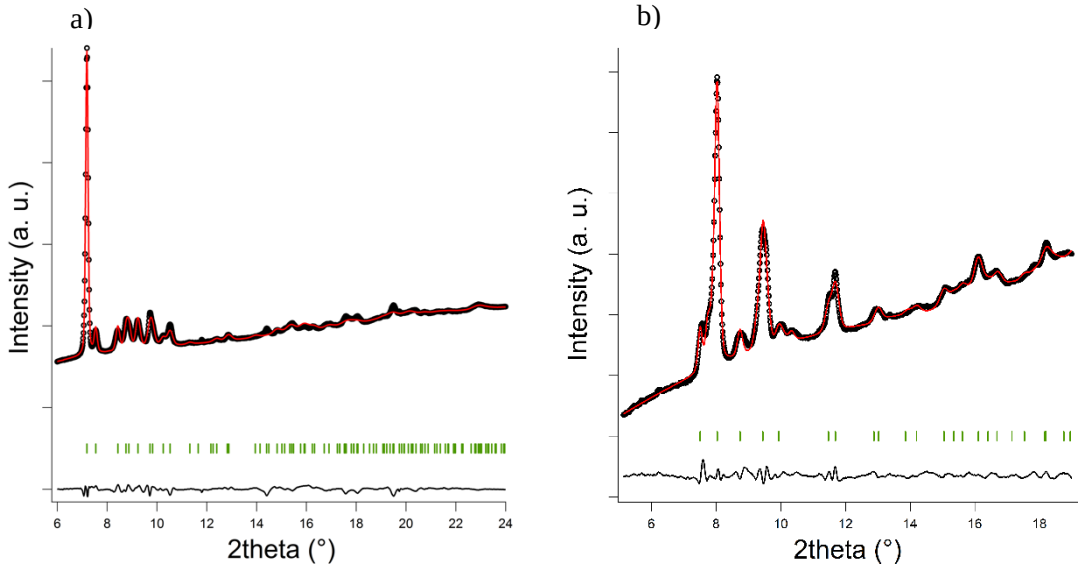

Figure S1. Diffraction pattern of a) the ε-phase obtained during decompression at 0.2 GPa and b) the ζ-phase, with the result of Rietvield refinement.

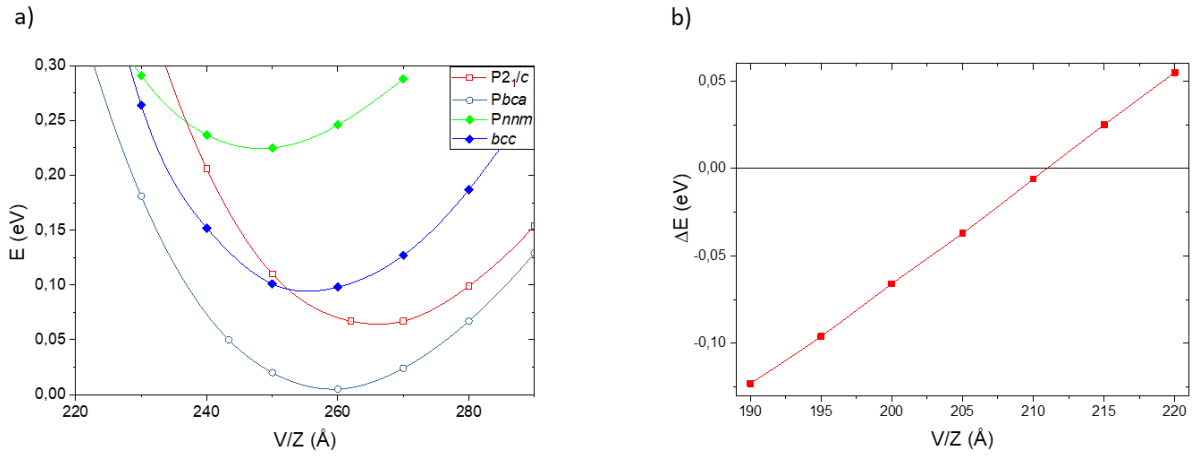

Figure S2. a) Calculated energy difference with respect to volume per formula unit for $P2_1/c$, *Pbca* structures, based on experimental refinement. The *bcc* anion packing corresponds to the *Im-3m* high temperature phase (without cation disorder) and *Pnnm* is the high-pressure structure with Na-Na dimers. The *Pbca* structure has the lowest ground state energy in the wide volume/pressure range. b) The energy difference between $Na_2B_{12}H_{12}$ in *Pbca* and *Pnnm* crystal strucures. ΔE = E(*Pnnm*) – E(*Pbca*). Below specific volume ~210 $Å^3$ the *Pnnm* phase is energetically favored.

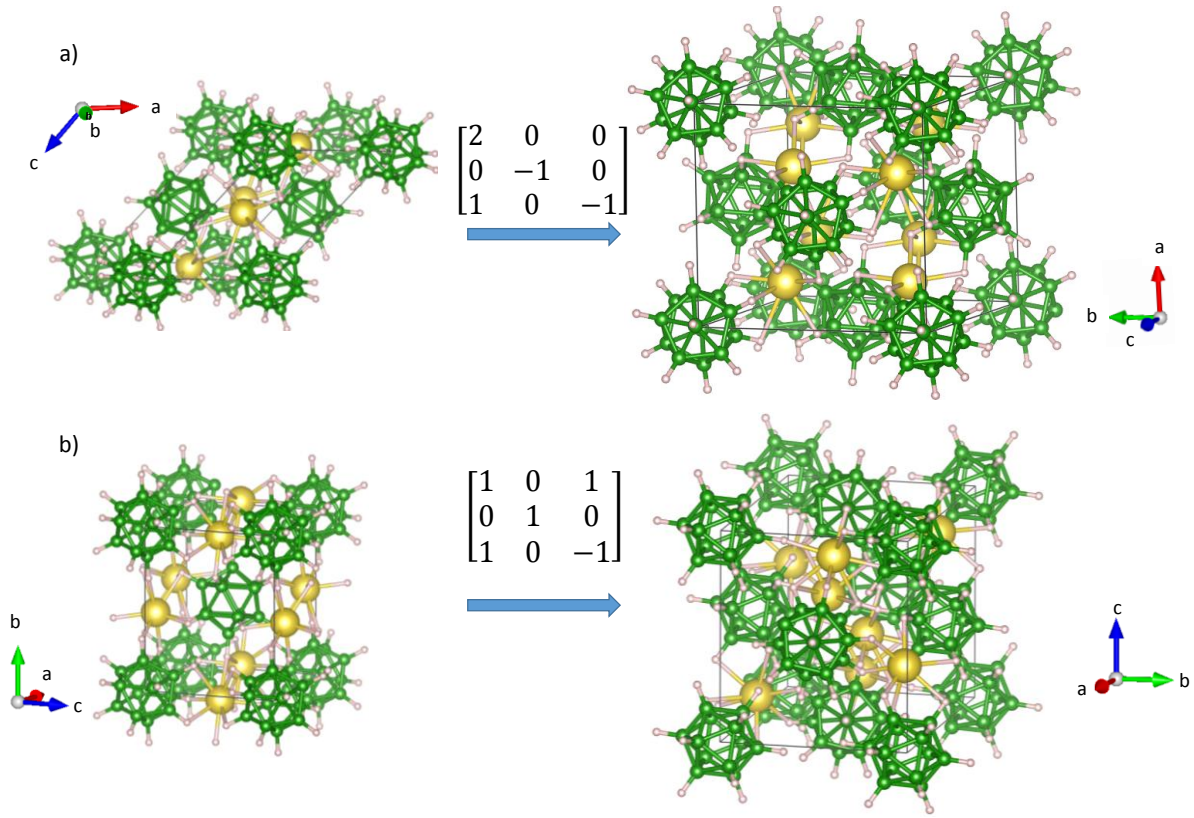

Figure S3. Transformation of the a) α-phase and b) ζ-phase into *fcc* packing. Boron (green), hydrogen (white), and sodium (yellow).

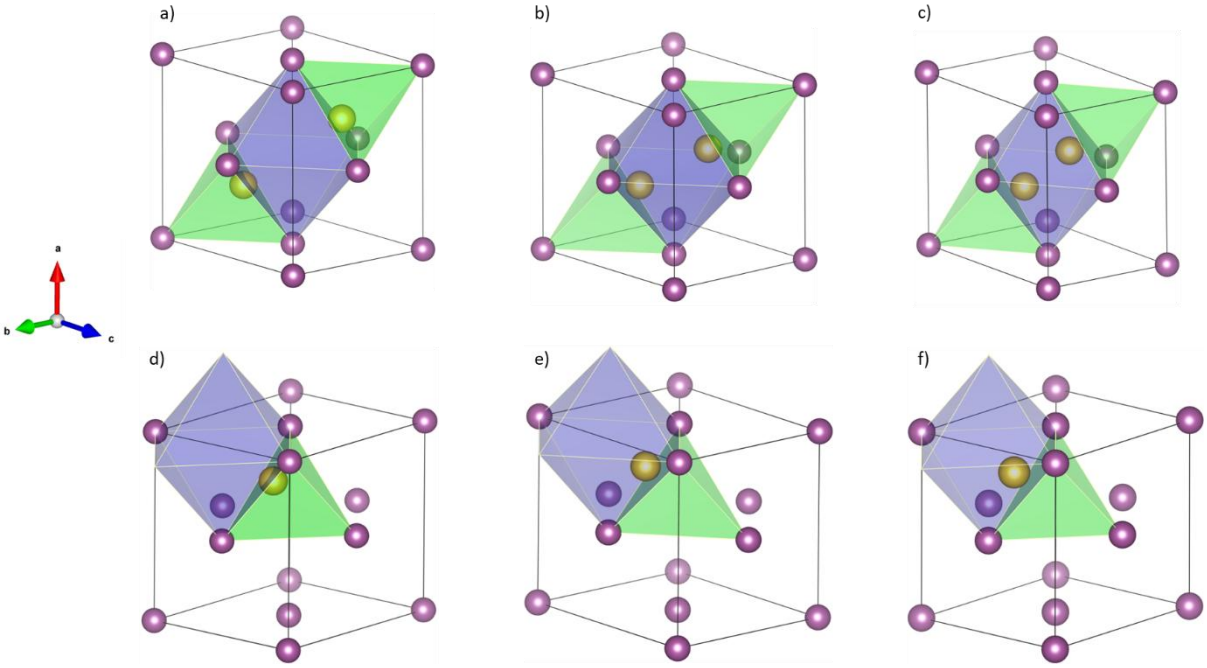

Figure S4. Representation of the environment for the 1st Na^+ (yellow) surrounded by $B_{12}H_{12}^{2-}$ units (purple) for a) α-phase, b) ε-phase and c) ζ-phase and for the 2nd Na^+ coordinated by $B_{12}H_{12}^{2-}$ units for d) α-phase, e) ε-phase and f) ζ-phase.

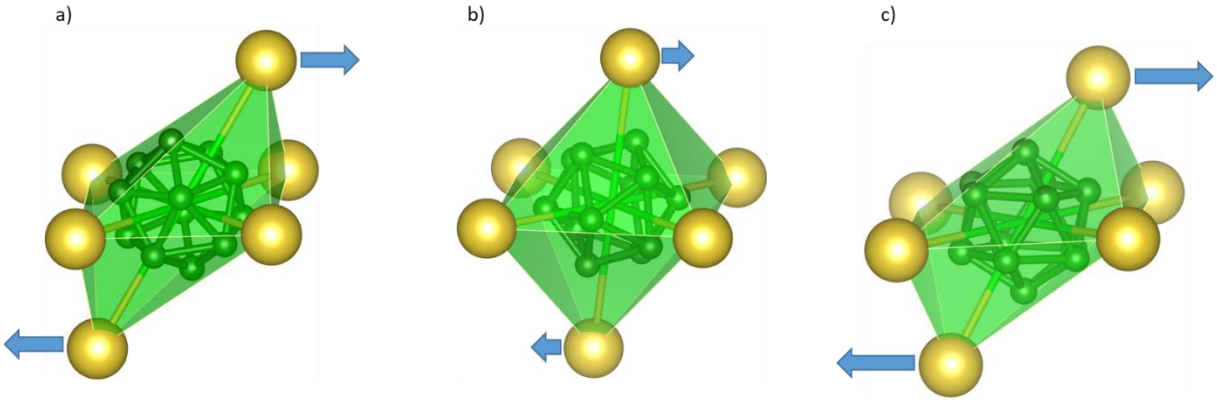

Figure S5. Representation of the distorted octahedral environment for $B_{12}H_{12}^{2-}$ units coordinated by Na^{+} for a) α-phase, b) ε-phase and c) ζ-phase.

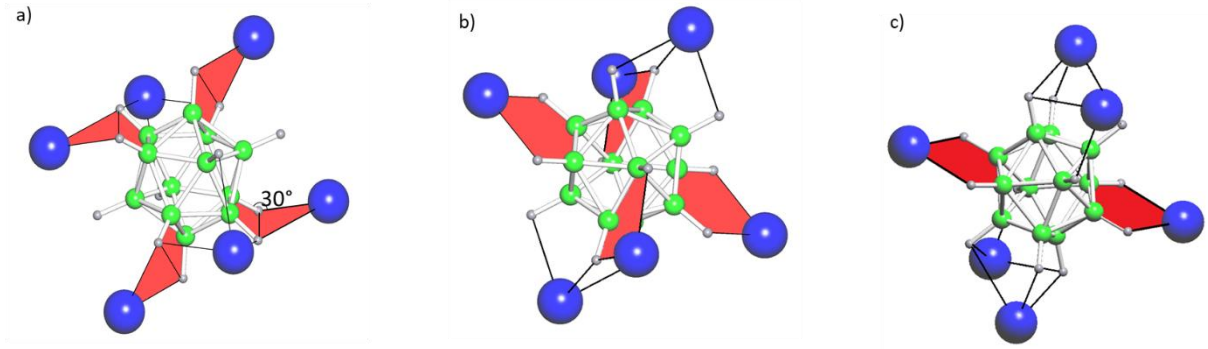

Figure S6. Representation of the Na^{+} coordination (blue) with the edges (red) and the faces (solid line) of $B_{12}H_{12}^{2-}$ (green) for a) α-phase, b) ε-phase and c) ζ-phase.

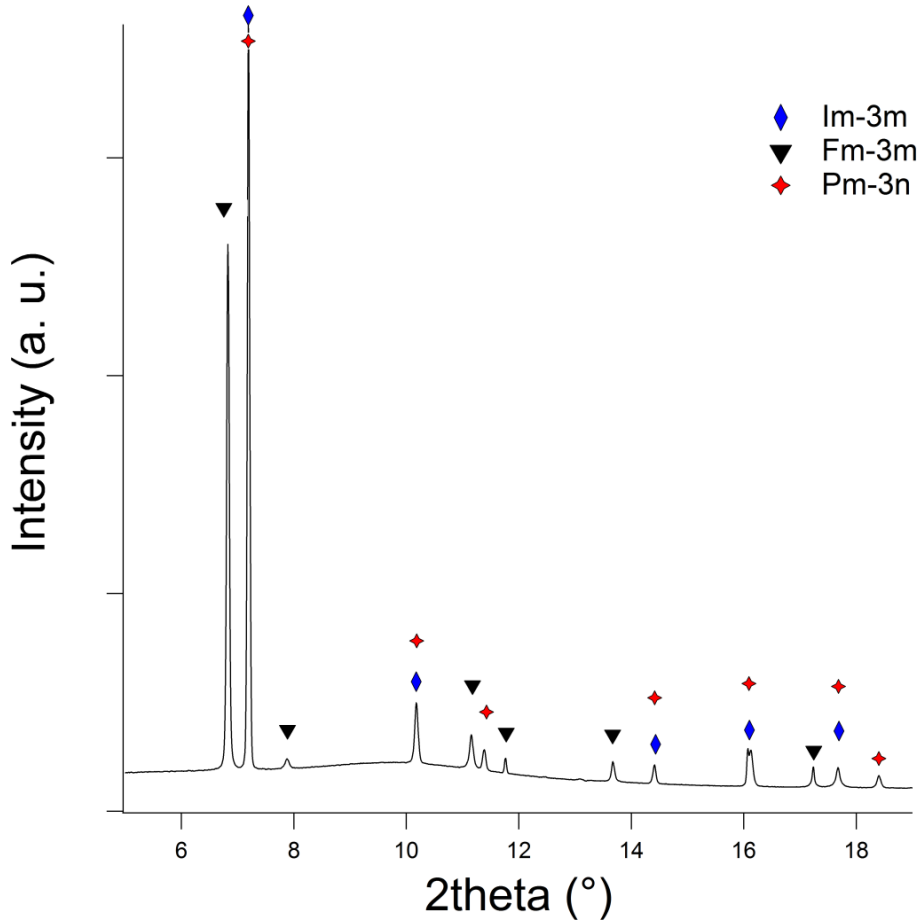

Figure S7. Diffraction pattern of $Na_2B_{12}H_{12}$ at 563K and assignation of the different phases. At this temperature, only the *Fm*-3*m* and *Pm*-3*n* phases are found. However, we added the position of the *Im*-*3m* phase in order to see which peaks disappears during the second transition (*Pm*-3*m* → *Im*-3*m*) corresponding to the forbidden reflections for the *Im*-3*m* symmetry (210) at 11.4° and the (320) at 18.4°.

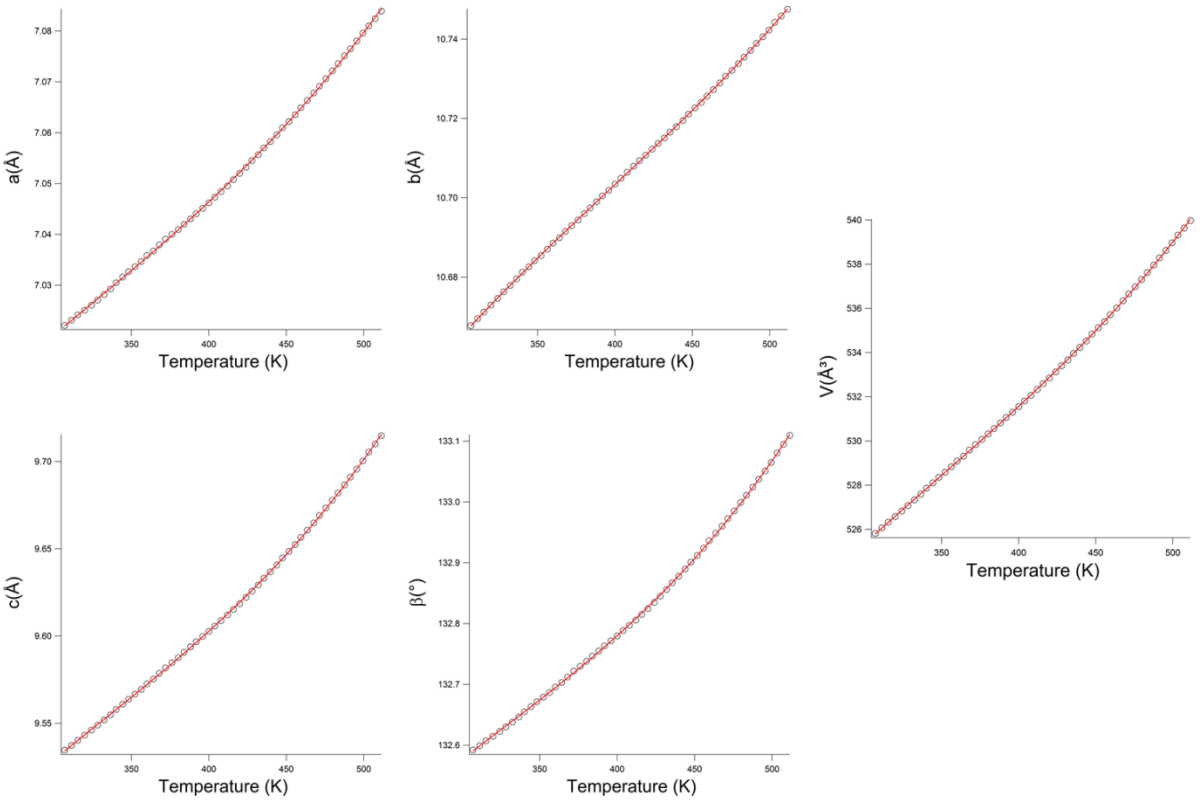

Figure S8. Lattices parameters evolution of α-Na2B12H12 as a function of temperatures. Empty circles: experimental, red line: fit.

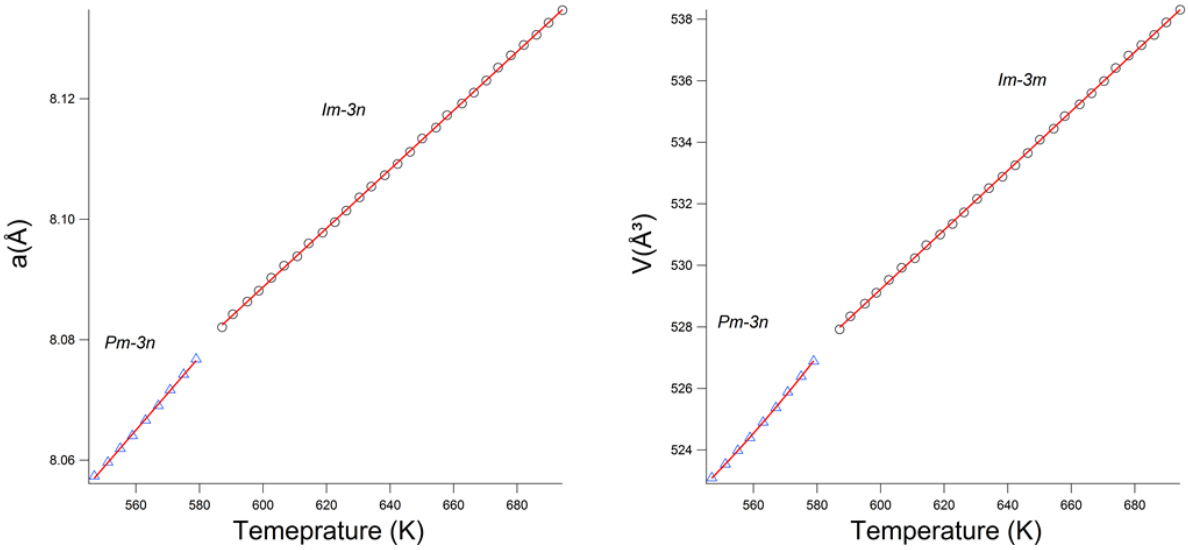

Figure S9. Lattice parameters evolution of β- and γ-$Na_2B_{12}H_{12}$ as a function of temperatures. Empty triangle and empty circles: Experimental linear fit (red).

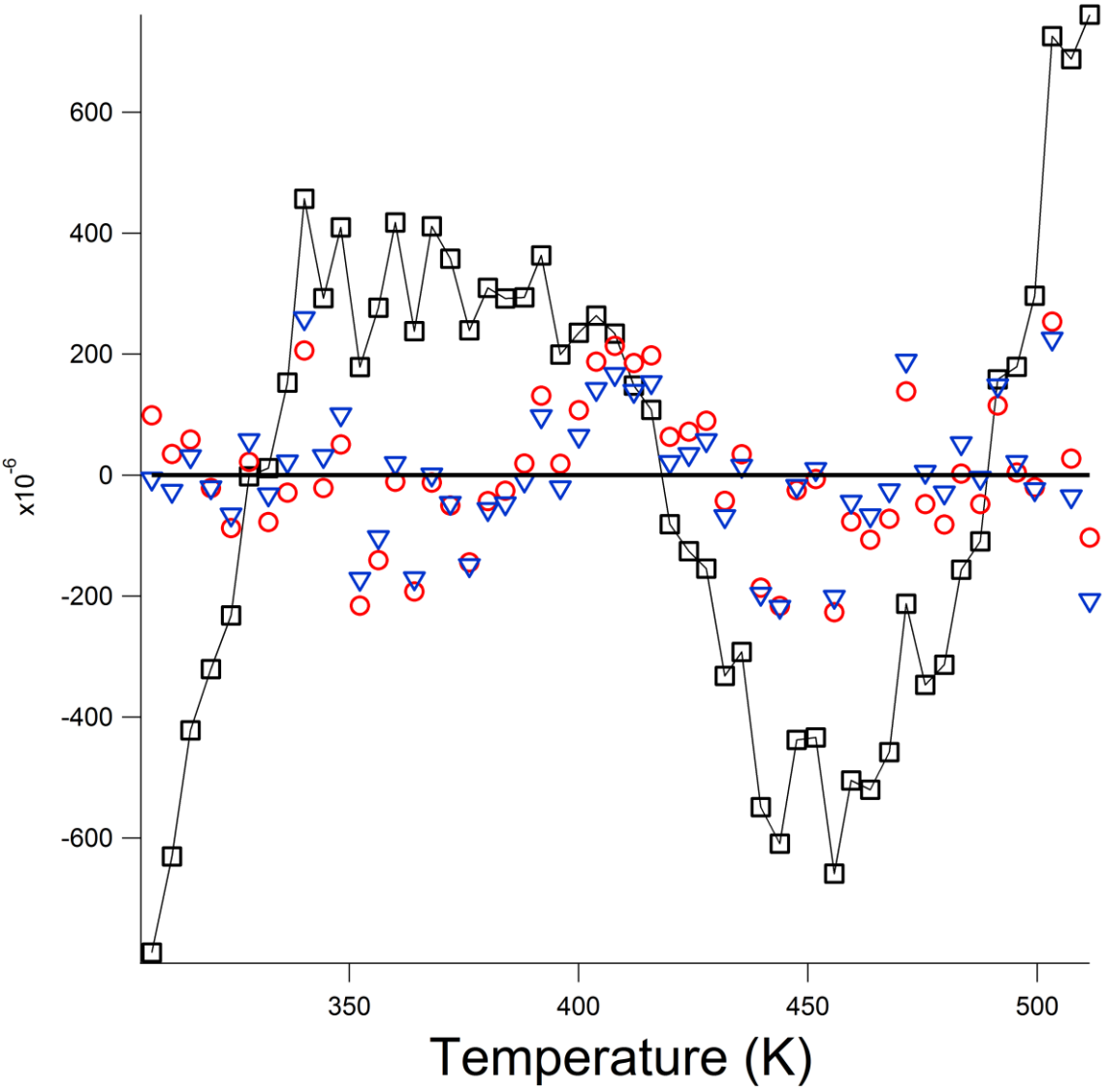

Figure S10. Comparison of the residual of the polynomial fit made on b as function of T for the LT phase as an example. Different polynomial orders have been applied: black squares 2nd order, red circles 3rd order, and blue triangle 4th order. It can be observed that a 2nd order polynomial does not estimate properly the evolution of the cell parameter b as a function of the temperature. Further, the trend and a 4th order polynomial doesn't improve the fit. Then, a 3rd order polynomial was chosen to fit all the curves. This trend is the same for the other parameters.

Table S1. Equation of the cell parameters evolution as a function of temperature for the LT- and HT-$Na_2B_{12}H_{12}$.

		Equation
P2₁/c	a (Å)	$6.90 + 6.42.10^{-4}T - 1.25.10^{-7}T^2 + 1.34.10^{-9}T^3$
	b (Å)	$10.42 + 1.37.10^{-3}T – 2.55.10^{-6}T^2 + 2.15.10^{-9}T^3$
	c (Å)	$9.12 + 2.49.10^{-3}T - 5.45.10^{-6}T^2 + 5.58.10^{-9}T^3$
	β (°)	$131.45 + 7.1.10^{-3}T - 1.63.10^{-6}T^2 + 1.71.10^{-8}T^3$
	V (Å^3)	$492 + 0.19T – 3.8.10^{-4}T^2 + 3.67.10^{-7}T^3$
Pm-3m	a (Å)	$7.72 + 6.1.10^{-4}T$
	V (Å^3)	$457.9 + 1.2.10^{-1}T$
Im-3m	a (Å)	$7.79 + 4.9.10^{-4}T$
	V (Å^3)	$471.4 + 2.4.10^{-4}T$

Table S2. Summary of the physical properties for the different known phases of $Na_2B_{12}H_{12}$

	α	β	γ	δ	ε	ζ
Space group	*P2₁/c*	*Pm*-3*n*	*Im*-3*m*	*Fm*-3*m*	*Pbca*	*Pnnm*
a	7.083915	8.05511	8.134716	10.3950	9.71959	6.30201
b	10.747533	8.05511	8.134716	10.3950	10.8522	8.67046
c	9.714884	8.05511	8.134716	10.3950	9.22670	7.01125
β	133.10928	X	X	X	X	X
T range[1]	RT-540K	511-587K	587-700K	587-700K	X	X
P range[2]	0-0.5GPa	X	X	X	0.5-5.7GPa[3]	>8.1GPa
α (K^{-1}) {T}	116.10^{-6} {300K}	227.10^{-6} {560K}	181.10^{-6} {640K}	X	X	X
B_0 (GPa)	17.3*	X	X	X	14, 15.4*	14*
G (GPa)	3.3*	X	X	X	6.9*	3.7*

*Values obtained by DFT calculations as describe in the text